Heliyon 9 (2023) e13648

Contents lists available at ScienceDirect

Heliyon

journal homepage: www.cell.com/heliyon

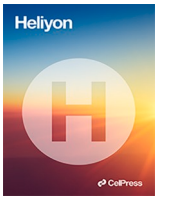

Research article

PANI-wrapped $BaFe_{12}O_{19}$ and $SrFe_{12}O_{19}$ with rGO composite materials for electromagnetic interference shielding applications

G.P. Abhilash [a], Devansh Sharma [b], Suryasarathi Bose [b], C. Shivakumara [a,*]

[a] Solid State and Structural Chemistry Unit, Indian Institute of Science, Bangalore, 560012, India
[b] Department of Materials Engineering, Indian Institute of Science, Bangalore, 560012, India

ARTICLE INFO

Keywords:
$BaFe_{12}O_{19}$
$SrFe_{12}O_{19}$
Polymer composites
In-situ polymerization
EMI shielding
Magnetic properties

ABSTRACT

We report electromagnetic interference (EMI) shielding efficiency in the PANI-wrapped $BaFe_{12}O_{19}$ and $SrFe_{12}O_{19}$ with rGO composites. Barium and strontium hexaferrites were synthesized using the nitrate citrate gel combustion method. These hexaferrites were polymerized *in situ* with aniline. The PANI-coated ferrite-based composite materials were developed along with reduced graphene oxide (rGO) in acrylonitrile butadiene styrene (ABS) polymer, and their shielding effectiveness was assessed in X-band frequency range (8.2–12.4 GHz). The reflection (SE_R) and absorption (SE_A) mechanism of shielding effectiveness was discussed with the different rGO concentrations. The results reveal that 5 wt% of rGO with PANI-coated barium and strontium hexaferrite polymer composites exhibit shielding efficiency of 21.5 dB and 19.5 dB, respectively, for 1 mm thickness composite. These hexaferrite polymer-based composite materials can be used as an attractive candidate for EM shielding materials in various technological applications.

1. Introduction

Wide use of electronic devices in automotive, digital assistants, and communication devices generates radiation, which interferes with the nearby electronic circuits and leads to electromagnetic interference (EMI). EMI harms the vital functioning and efficiency of electronic devices and military applications [1–3]. It also incurs harmful effects on health and the environment [4]. EMI is a major concern of modern society, and thus, it is critical to protect electronic devices from EMI. This can be achieved by developing materials that effectively shield the EMI signal to protect the electronic components of devices. Therefore, shielding materials that attenuate EMI signal has become a focal point of research, even in the industrial sector.

Shielding material attenuates EM signal mainly in two ways shielding by reflection (SE_R) and shielding by absorption (SE_A). Reflection occurs due to the interaction of electromagnetic radiation with the free charge present on the surface of a material; it is due to impedance mismatch between air and the surface of a material. Whereas absorption is caused by the interaction of electric and magnetic dipoles present in the materials [5,6]. Metals are suitable material that effectively shields the EM radiation because they possess free electrons on their surface and has high electrical conductivity [7]. However, the use of metals in EMI shielding applications is limited by properties, such as high density, low flexibility, poor resistance to corrosion, and difficulty processing the material. Therefore, polymer-based nanocomposites have gained interest due to their lightweight nature, easy processability, resistance to corrosion, and fine-tuning of desired properties of fillers with polymer matrix required for shielding applications [8]. Therefore,

* Corresponding author.
E-mail address: shiva@iisc.ac.in (C. Shivakumara).

https://doi.org/10.1016/j.heliyon.2023.e13648
Received 9 November 2022; Received in revised form 7 February 2023; Accepted 7 February 2023
Available online 11 February 2023

research focused on development of materials that overcome the above-mentioned disadvantages of metals has gained traction.

A shielding material having electric and magnetic dipoles can shield by interacting with electric and magnetic components of EM waves [9,10]. Earlier, carbon-related materials such as multiwall carbon nanotube (MWCNT), graphene, carbon black, and reduced graphene oxide served reliably in electromagnetic shielding applications because of their lightweight nature, increased conductivity, and enhanced mechanical strength with high aspect ratio and flexibility [11–13]. These materials mainly absorb EM radiation through conduction loss, Thus, Composites containing both conducting and magnetic material will be more effective in shielding EM waves [14]. Therefore, addition of magnetic material enhances the EM absorption by an impedance mismatch between air and the surface of the material, resulting in EM waves entering into the material and getting absorbed [15]. Magnetic material like hexaferrite are used in EM shielding applications because of their high saturation magnetization (Ms) [16] and large Snoek's limit, at higher frequencies >1 GHz permeability decreases and approaches constant value unity beyond the limiting value of frequency. Due to weak magneto-crystalline anisotropy and attenuated permeability, the eddy current phenomenon limits their usage at high frequencies [17]. Therefore, coating these materials with conducting material could improve absorption ability by elevating surface anisotropy energy and limiting the eddy current [18,19]. Conducting polymer composites with hexaferrite increases the dielectric loss of a shielding material; polyaniline (PANI) coating enhances the shielding efficiency [20,21]. There are several studies are done on core-shell composites using PANI; the advantage of core-shell heterostructures is taken into account as shells to increase the effectiveness of their microwave shielding. Han et al. reported a 3-D porous nickel metal foam/PANI heterostructure for superior absorption-based EM shielding [22]. Yang and co-workers developed polyaniline-coated bagasse fiber composite with core-shell heterostructure for effective EM performance [23], they also reported the bending durability of flexible polyethylene terephthalate/polyaniline composite and their shielding performance [24]. Zhangjing et al. synthesized polyaniline on insulating bamboo fiber and studied the EM shielding behavior of composites [25]. Though there are several studies done on the EM shielding properties of these core–shell composites, more research is required to explain the effects of core materials on the electrical conductivity of the PANI shell and their underlying EMI shielding mechanisms, which are significant factors influencing the EMI shielding properties. Here we choose hexaferrite as a core material because their magnetic properties and insulating in nature make it ideal for coating the PANI layer to regulate conductivity [16].

This work uses a synergetic approach to attenuate EM waves using reduced graphene oxide (rGO) with PANI-coated hexaferrite and MWCNT to shield EM waves. rGO was synthesized using graphite and oxidized to graphene oxide (GO) by modified Hummer's method. Subsequently, GO was chemically reduced using hydrazine hydrate to obtain rGO. Hexaferrites were synthesized by nitrate citrate gel combustion method and were coated with PANI by *in-situ* emulsion polymerization of aniline. Different weight ratios of rGO with PANI-coated hexaferrite were incorporated in acrylonitrile butadiene styrene (ABS) matrix with MWCNT by using the solution casting method, and samples were compression-molded at 230 °C to get uniform films. The morphology, magnetic properties, coercivity and

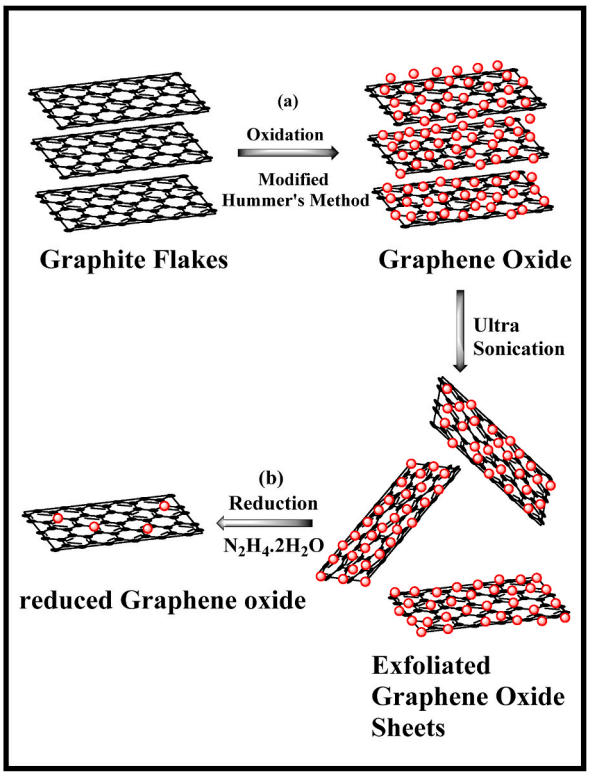

Scheme 1. Synthesis of (a) graphene oxide and (b) reduced graphene oxide.

saturation magnetization of hexaferrite and their PANI-coated composites were studied. Furthermore, the effect of adding different weight percentages of rGO on the microwave absorption efficiency in the resultant ternary composites was also studied.

2. Experimental section

2.1. Materials

Pristine MWCNTs length NC 7000 (1.5 μm and diameter 9.5 μm) were obtained from Nanocyl SA (Belgium). Graphite and acrylonitrile butadiene styrene (ABS) were procured from Sigma-Aldrich (USA). Barium nitrate $Ba(NO_3)_2$, sodium nitrate $Na(NO_3)_2$, ferrous nitrate $Fe(NO_3)_2$, ammonium persulphate, aniline ($C_6H_5NH_2$), hydrogen peroxide (H_2O_2), ethanol, acetone, and tetrahydrofuran (C_6H_8O) were purchased from commercial sources.

2.2. Synthesis of graphene oxide (GO)

Graphene oxide was synthesized using modified Hummer's method [26,27] which involves the oxidation of graphite into graphene oxide. Briefly, 1 g of graphite flakes were added to a 9:1 ratio of H_2SO_4 and H_3PO_4, followed by ultra-sonication for about 30 min. To this, 4 g of $KMnO_4$ was added slowly by maintaining the reaction temperature below 10 °C using an ice bath. Then the reaction mixture was heated at 65 °C for 4 h. The mixture was poured into ice-cold water taken in a beaker; a bright yellow-brown color precipitate is formed. To this, 10 ml of H_2O_2 was added for the complete oxidation of $KMnO_4$. The obtained precipitate was treated with 1 M HCl solution and finally washed with distilled water and ethanol. The resulting product, graphene oxide (GO), was dried at 40 °C in a vacuum oven (Scheme 1a).

2.3. Synthesis of reduced graphene oxide (rGO)

1 mg/ml of GO was dissolved in distilled water was taken in a beaker and ultra-sonicated for an hour. To this, 15 μL of hydrazine hydrate was added along with few drops of ammonium hydroxide. The reaction mixture was heated for about 12 h at 90 °C with constant stirring [28,29]. The black precipitate was washed with distilled water, followed by acetone. The final compound, reduced graphene oxide (rGO), was dried at 90 °C in a vacuum oven. (Scheme 1b).

2.4. Synthesis of $BaFe_{12}O_{19}$ and $SrFe_{12}O_{19}$

$BaFe_{12}O_{19}$ and $SrFe_{12}O_{19}$ were prepared by nitrate citrate gel combustion method. In a typical synthesis of $BaFe_{12}O_{19}$, barium nitrate and ferric nitrate was taken in the ratio of 1:11 and dissolved in a distilled water. To this, citric acid (CA) was added to form

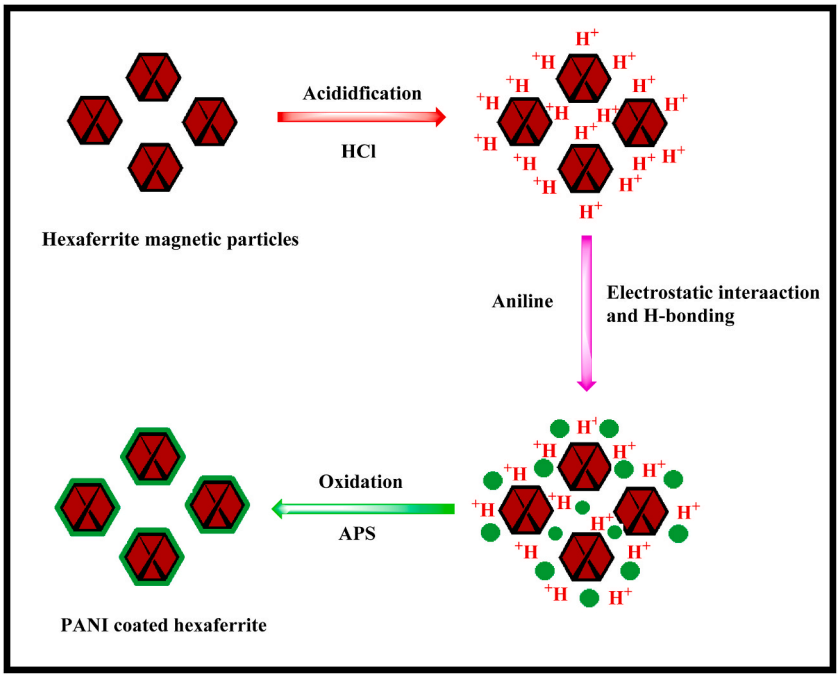

Scheme 2. Polymerization of magnetic nanoparticles.

chelate with Ba^{2+} and Fe^{3+} ions, such that the mole ratio of CA to nitrate solution was maintained at 1:1. The mixture was maintained at pH 7 by adding dilute ammonia solution, and the beaker was kept on a hot plate with constant stirring at 150 °C. When the solution became viscous, the temperature was raised to 200 °C; at this stage, the gel gets ignited and burnt to form a brown-colored powder. The obtained powder was calcined at 1000 °C for 2 h, with a heating rate of 10 °C/min to get hexagonal ferrite phase [30,31]. Similar procedure was adopted to prepare the $SrFe_{12}O_{19}$ phase by using strontium nitrate in place of barium nitrate.

2.5. Synthesis of PANI-coated $BaFe_{12}O_{19}$ and $SrFe_{12}O_{19}$ composites

The synthesized magnetic hexaferrites, $BaFe_{12}O_{19}$ and $SrFe_{12}O_{19}$ were *in-situ* polymerized using aniline. For this, 0.1 g of $BaFe_{12}O_{19}$ was added in a round-bottom flask containing 40 ml of 0.1 M HCl solution. The suspension was ultrasonicated for about 10 min and kept in the ice bath for 10 h at 5 °C to settle down the particles. Subsequently, the HCl solution was decanted to isolate the particles. 10 ml anhydrous ethanol and 0.1 ml of aniline were added to the particles, and the mixture was subjected to ultrasonication for 10 min to obtain a uniform dispersion of the particles. Following this, the mixture was placed in an ice bath for 12 h at 5 °C. 0.17 ml of 12 M HCl was then added to this mixture, followed by dropwise addition of APS aqueous solution (0.04 M, 30 ml). The mixture was constantly stirred for 3 h. The obtained product was collected and washed with distilled water and ethanol several times and dried in a vacuum oven [32,33]. Similar experimental procedure was employed to prepare strontium hexaferrite-PANI composite, using strontium hexaferrite in place of barium hexaferrite (Scheme 2).

2.6. Preparation of rGO/PANI-hexaferrite/MWCNT/ABS nanocomposites

Synthesized rGO, PANI-coated hexaferrite, and MWCNT were taken in a separate beaker and probe sonicated with tetrahydrofuran (THF) for 20 min to remove primary agglomerates and bath sonicated for another 20 min to remove secondary agglomerates. On the other hand, ABS polymer was dissolved in THF solution. The solutions of rGO, PANI-coated hexaferrite, and MWCNT were added into the dissolved ABS and sonicated for 1 h. The obtained solution was poured into a glass Petri dish and kept overnight for solvent evaporation. The formed polymer composites were subjected to compression-molding at 230 °C to get uniform films.

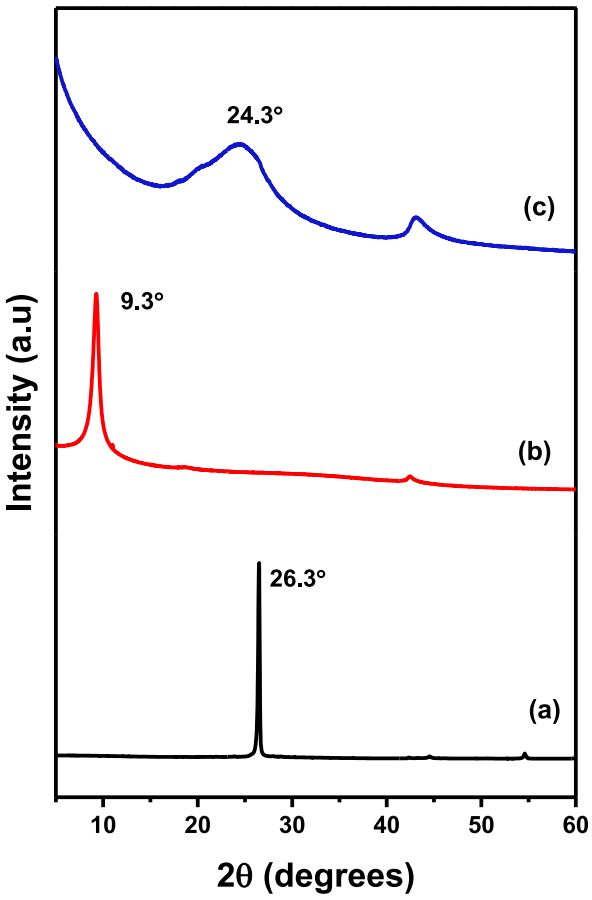

Fig. 1. XRD patterns of (a) Graphite, (b) GO, and (c) rGO.

2.7. Characterization

Powder X-ray diffraction pattern (PXRD) was recorded to determine the phase purity by using a PANalytical X'Pert diffractometer of Cu Kα source (λ = 1.5418 Å) Ni-filter at operating voltage 45 kV and current 30 mA. A Fourier-transform infrared spectroscopy (FTIR) spectrum was recorded by using a PerkinElmer Spectrum 1000. A field emission scanning electron microscope (FESEM, ULTRA 55), at an accelerating voltage of 15 kV, was used to get the morphology of the prepared materials and composites. Thermal analysis was done using Mettler Toledo system using N_2 as a carrier gas up to 600 °C with an incremental 5 °C step size to determine the stability of the prepared sample. A lakeshore vibrating sample magnetometer (VSM) was used to determine the magnetic properties of the prepared hexaferrite materials with applied force −50000 to 50000 Oe at room temperature. Electromagnetic interference shielding was studied using Keysight N9921A vector network analyzer that uses corresponding waveguide in the frequency range 8.2–12.4 GHz (X-band). Before measuring, SE full setup was calibrated by SOLT (short-open-load-through). For most measurements, a rectangular sample of 5 mm thickness prepared by compression molding at 230 °C was used. The S parameters obtained from VNA (Vector Network Analyzer) measurements were used to calculate SE_R, SE_A, and SE_T.

3. Results and discussion

3.1. Structure, functional and morphological properties of prepared composite materials

Powder X-ray diffraction (XRD) patterns of (a) graphite, (b) GO, and (c) rGO are shown in Fig. 1. The intense sharp peak (002) of graphite was observed at 2θ value of 26.3° with interlayer d-spacing of 0.33 nm (Fig. 1a) Upon oxidation, the graphite peak shifted to lower 2θ at 9.3° with interlayer spacing 0.94 nm (Fig. 1b), indicating the oxidation of graphite to graphene oxide. After the chemical reduction of GO with hydrazine hydrate, the diffraction peak at 9.3° disappeared and shifted to a higher angle with a broader peak around 2θ value 24° (Fig. 1c), which confirms the formation of reduced graphene oxide (rGO) [34,35]. The results obtained from XRD analyses of graphite, GO and rGO are in agreement with the reported literature [27]. To determine whether the hexaferrite undergo a structural or phase change by polymerization with aniline, the base chemicals ($BaFe_{12}O_{19}$ and $SrFe_{12}O_{19}$) and their polyaniline (PANI) derivatives were subjected to powder X-ray diffraction analysis. All the diffracted peaks in the powder X-ray diffraction pattern of barium hexaferrite ($BaFe_{12}O_{19}$) are well-matched with M-type barium hexaferrite (JCPDS card no. 43–0001) (Fig. 2i, lower panel) After polymerization of $BaFe_{12}O_{19}$ particles with PANI, a slight decrease in the intensity is observed in the $BaFe_{12}O_{19}$-PANI composite, due to the amorphous coating of aniline (Fig. 2i, upper panel), which confirms that there is no change in the crystal structure of barium hexaferrite [36]. Similarly, in the powder X-ray diffraction pattern of strontium hexaferrite ($SrFe_{12}O_{19}$), the diffraction peaks are well-matched with the JCPDS card No. 80–1197 (Fig. 2ii, lower panel). The observed pattern is ascribed to M-type strontium hexaferrite. After polymerization with PANI, no change was observed in the diffraction pattern, except a small decrease in the peak

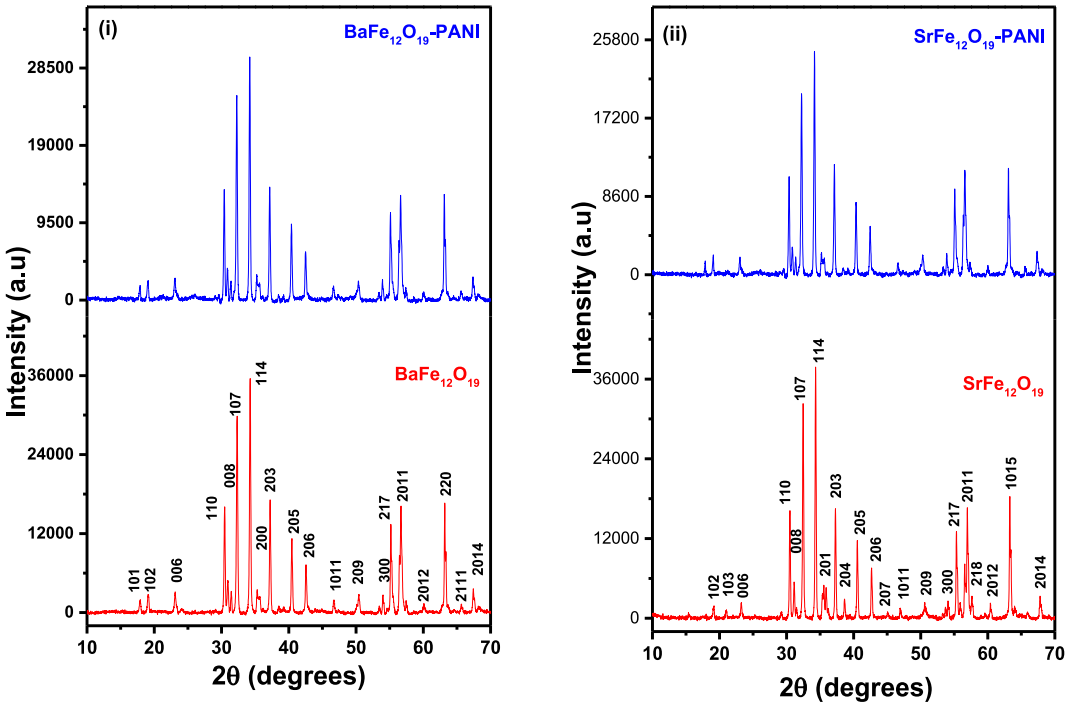

Fig. 2. XRD patterns of (i) $BaFe_{12}O_{19}$ and $BaFe_{12}O_{19}$-PANI composite and (ii) $SrFe_{12}O_{19}$ and $SrFe_{12}O_{19}$-PANI composite.

intensities (Fig. 2ii, upper panel) [37], which shows that *in situ* polymerization with PANI does not affect the phase of hexaferrites. Thus, powder X-ray diffraction analysis confirmed that addition of PANI to the hexaferrites does not affect the basic structure or phase of the hexaferrites. Fig. S1, shows PXRD of bare ABS and ABS with prepared fillers, which infers that after incorporation of fillers in ABS polymer matrix, there is no structural change in the PANI coated hexaferrite, which signifies PANI layer does not peel off from the surface of hexaferrite during polymer composite preparation.

Fig. 3 shows the FTIR spectra of GO and rGO. Upon oxidation of graphite, oxygen-based functional groups are attached to the graphite layers. In the spectra of GO, the peak at 1580 cm^{-1} corresponds to C═C in plane stretching vibrations of sp^2 hybridized carbon atoms (Fig. 3a). Likewise, peaks for C═O (1720 cm^{-1}), C–O (1050 cm^{-1}), and C–O–C (1220 cm^{-1} and 846 cm^{-1}) corresponds to asymmetric stretching and bending modes, respectively (Fig. 3a). In the FTIR spectra of rGO, the peak at 1578 cm^{-1} corresponds to C–C stretching mode indicating restoration of sp^2 regions, and the disappearance of peak at 1731 cm^{-1} confirms reduction of C═O groups (Fig. 3b). Absence of other peaks indicate the effective reduction of graphene oxide (Fig. 3b) [38,39]. Thus, oxidation of graphite and reduction of graphene oxide was confirmed using FTIR spectra analysis.

Fig. 4 shows the FTIR spectra of hexaferrite, PANI, and PANI-coated hexaferrite. In the curve for $BaFe_{12}O_{19}$ (Fig. 4i a), the absorption peaks at 570 cm^{-1} and 538 cm^{-1} corresponds to the vibrational stretching frequency of tetrahedral site of Fe and O, and the one at 420 cm^{-1} is for the vibrational stretching frequency of octahedral site. These three characteristic absorption peaks indicate the structure of M type hexaferrite [40]. Similar vibrational bands were observed for $SrFe_{12}O_{19}$ (Fig. 4 ii a). The curve for $BaFe_{12}O_{19}$-PANI composite shows characteristic peaks of both PANI and the hexaferrite (Fig. 4 i a and c). The peak at 1586 cm^{-1} corresponds to C═N stretching vibration of the benzenoid or quinoid ring; the peak at 1495 cm^{-1} is assigned to C═C of the benzenoid or quinoid ring; the peaks at 1298 and 1238 cm^{-1} are from the C–N stretching vibration of the benzenoid ring; 1114 cm^{-1} peak corresponds to the in-plane bending vibration of the C–H quinoid ring and the peak at 816 cm^{-1} is due to the out-of-plane bending vibration of C–H and N–H of the benzenoid or quinoid unit [41]. Furthermore, the characteristic peaks of hexaferrites at 570 cm^{-1}, 538 cm^{-1} and 420 cm^{-1} are also observed (Fig. 4i b). Similar results obtained for $SrFe_{12}O_{19}$-PANI composite shown in (Fig. 4 ii a, b and c). Thus, these FTIR spectra confirm the chemical bonds formed in the PANI-coated hexaferrite composites. FTIR spectra of ABS polymer along with ABS with fillers are given in Fig. S2.

Thermogravimetric analysis (TGA) measurement gives the information about the decomposition temperature and stability of samples. Fig. 5 shows TGA plots for (a) Graphite, (b) GO, and (c) rGO samples, Curve (a) shows graphite powder which does not undergo weight loss up to 600 °C, indicates the stability of graphite (Fig. 5, curve a). Curve (b) represents the GO sample, in which

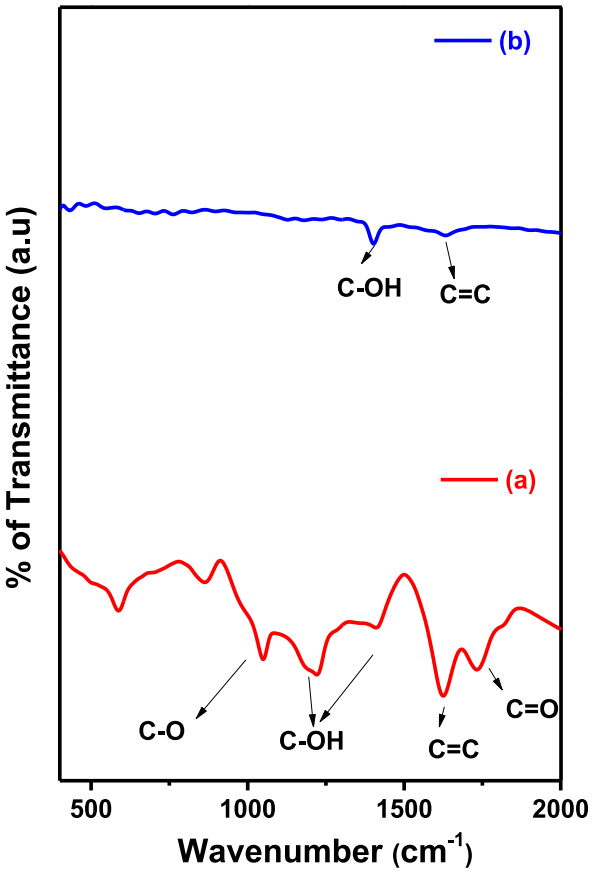

Fig. 3. FTIR spectra of (a) GO and (b) rGO.

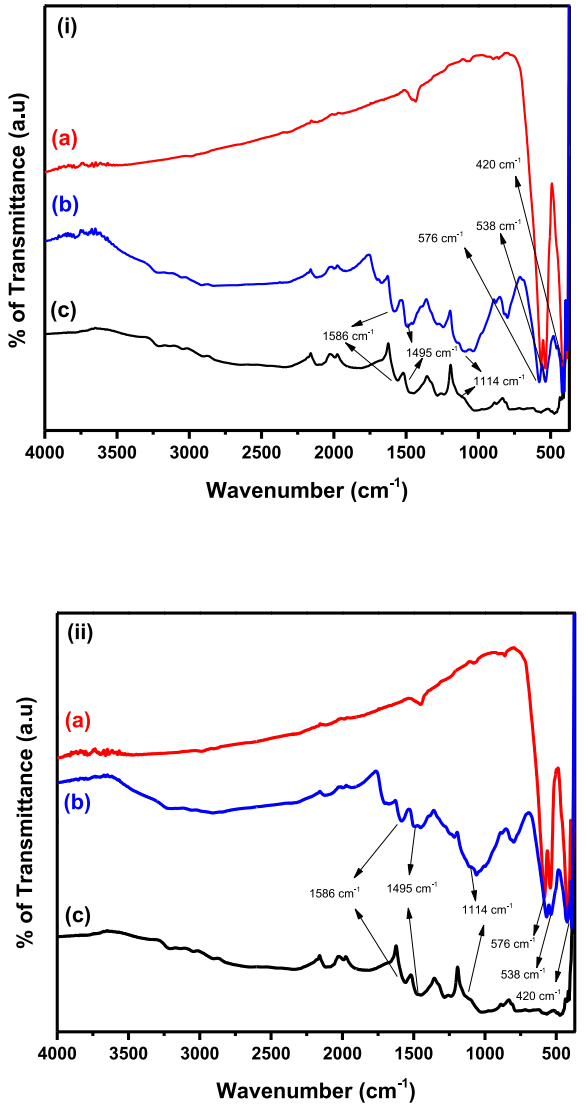

Fig. 4. FTIR spectra of (i) (a) $BaFe_{12}O_{19}$, (b)$BaFe_{12}O_{19}$-PANI, (c) PANI, (ii) (a) $SrFe_{12}O_{19}$, (b) $SrFe_{12}O_{19}$-PANI and (c) PANI.

weight loss is observed at three stages (Fig. 5, curve b). The first stage observes around 20% weight loss (at 150 °C) due to the removal of adsorbed water molecules. In the second stage, a further weight loss of about 25% takes place due to the removal of functional groups like –OH, C═O, and C–O–C which escape from layers of GO forming CO_2, CO, and steam. Finally, a mass loss of 15% occurs due to pyrolysis of the carbon skeleton. Curve (c) depicts the rGO sample, which shows an initial weight loss of approximately 24% occurring between 25 °C to 150 °C because of removal of the adsorbed water molecule and residual functional groups present in the sample (Fig. 5, curve c). After this initial weight loss, rGO does not lose any appreciable weight and behaves like a pristine graphite sample (Fig. 5, curve c) [42,43]. From TGA graph it is confirms that, the synthesized GO and rGO shows their characteristic behavior which are reported in the literature. TGA graph of prepared ABS polymer composites are shown in Fig. S3, which shows prepared polymer composites can withstand temperature up to 300–350 °C.

Fig. 6 shows the FESEM images of (a) $BaFe_{12}O_{19}$ and (c) $SrFe_{12}O_{19}$ compounds. The electron micrographs of both barium and strontium hexaferrites, exhibit agglomerated morphology with dense packing of particles due to the magnetic dipole interaction between the ferrites (Fig. 6a and c) [44]. After polymerization, the surface of the hexaferrite is coated with aniline monomers being selectively adsorbed on the surface of the hexaferrite by electrostatic interaction forming H-bond (Fig. 6b and d) [45]. PANI-coated hexaferrites eventually form core-shell composite structures (Scheme 2). For elemental analysis of the samples, energy dispersive X-ray spectroscopy (EDS) was undertaken. EDS spectrum for (a) $BaFe_{12}O_{19}$, (b) $BaFe_{12}O_{19}$-PANI, (c) $SrFe_{12}O_{19}$, and (d) $BaFe_{12}O_{19}$--PANI revealed the atomic percentage of various elements present in the prepared samples (Fig. S4).

Fig. 7 depicts the room temperature magnetization as a function of applied field for $BaFe_{12}O_{19}$, $BaFe_{12}O_{19}$-PANI, $SrFe_{12}O_{19}$, and $SrFe_{12}O_{19}$-PANI composites. Fig. 7i reveals that, after coating of PANI, the value of saturation magnetization (Ms) decreased from 49.2

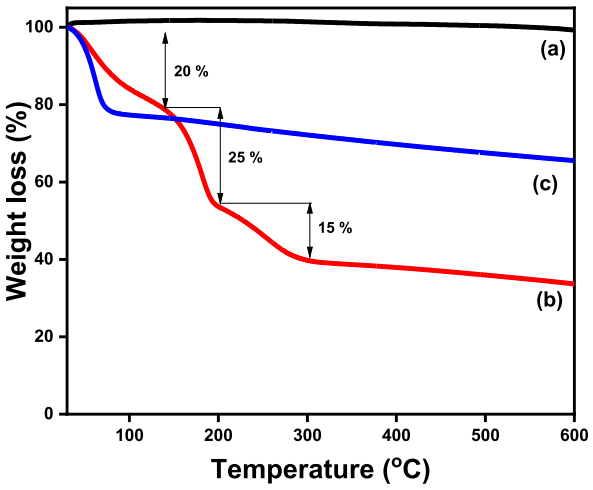

Fig. 5. TGA plot of (a) Graphite, (b) GO, and (c) rGO.

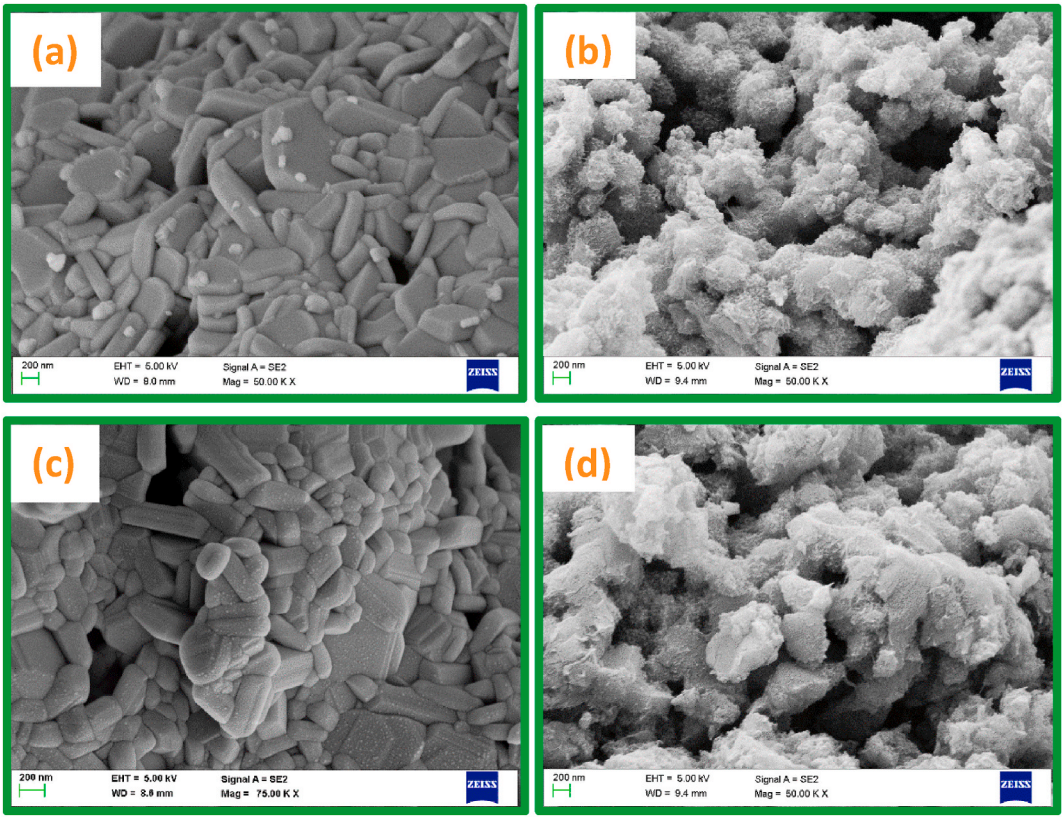

Fig. 6. FE-SEM micrographs of (a) $BaFe_{12}O_{19}$, (b) $BaFe_{12}O_{19}$/PANI, (c) $SrFe_{12}O_{19}$, and (d) $SrFe_{12}O_{19}$/PANI.

emu g^{-1} for $BaFe_{12}O_{19}$ to 14.8 emu g^{-1} for $BaFe_{12}O_{19}$-PANI (Fig. 7i). The remanent magnetization (Mr) values also decreased from 24 emu g^{-1} for $BaFe_{12}O_{19}$ to 7 emu g^{-1} for $BaFe_{12}O_{19}$-PANI (Fig. 7i). Reduction in the Ms and Mr values might be attributed to the decreased crystallinity of hexaferrite upon polymerization, which induces a spin disorder enhancement, thereby decreasing the saturation magnetization values. Intriguingly, there was no significant change in the coercivity (Hc) for both the samples from −50000 to +50000 Oe, which indicate that the hexaferrite retained its hard ferrimagnetic nature after polymerization. Similar behavior was observed for $SrFe_{12}O_{19}$, and $SrFe_{12}O_{19}$-PANI composites (Fig. 7ii). In Table 1, summarized the values of saturation magnetization, coercivity and remanent magnetization. The high coercivity value demonstrates high magnetic crystalline anisotropy, signifying a high anisotropy energy (Ha) and resonance frequency (fr) as deduced from the following relations [46].

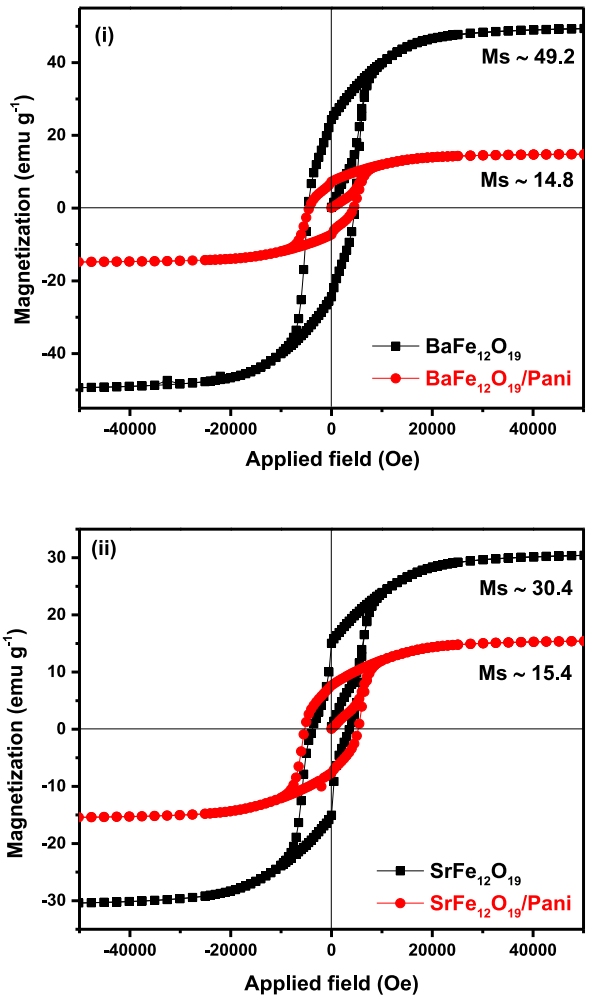

Fig. 7. Room-temperature magnetization curve of (i) $BaFe_{12}O_{19}$ and $BaFe_{12}O_{19}$/PANI and (ii) $SrFe_{12}O_{19}$ and $SrFe_{12}O_{19}$/PANI.

$$K = \frac{\mu_0 M_S H_C}{2}$$

$$Ha = \frac{4|K|}{3\mu_0 M_S}$$

$$2\pi f_r = rH_a$$

3.2. Raman spectroscopy

Raman spectra is a non-destructive technique used to study the structural elucidation of carbon materials like diamond, graphite, graphene oxide, reduced graphene oxide, and CNT. Raman spectra of GO and rGO are recorded and shown in Fig. 8. It shows characteristic D and G peaks at 1345 cm^{-1} and 1596 cm^{-1}, respectively (Fig. 8). The D band corresponds to defects that arise during the oxidation and reduction of carbon lattice of graphite, while the G band is a graphitic band associated with in-plane vibrations of C–C stretching E_{2g} band. Integrated intensity ratio (I_D/I_G) depicts disorders and is inversely proportional to the average size of defect-free sp^2 regions. I_D/I_G ratios of GO and rGO are 1.01 and 1.22, respectively (Fig. 8), suggesting that defect band intensity increases upon reduction of GO [42].

3.3. AC electrical conductivity of the composites

Electromagnetic shielding efficiency depends on the conductivity of the shieling materials. Fig. 9 shows the AC electrical conductivity versus frequency at room temperature. Incorporation of $BaFe_{12}O_{19}$-PANI and $SrFe_{12}O_{19}$-PANI results in an insulating matrix

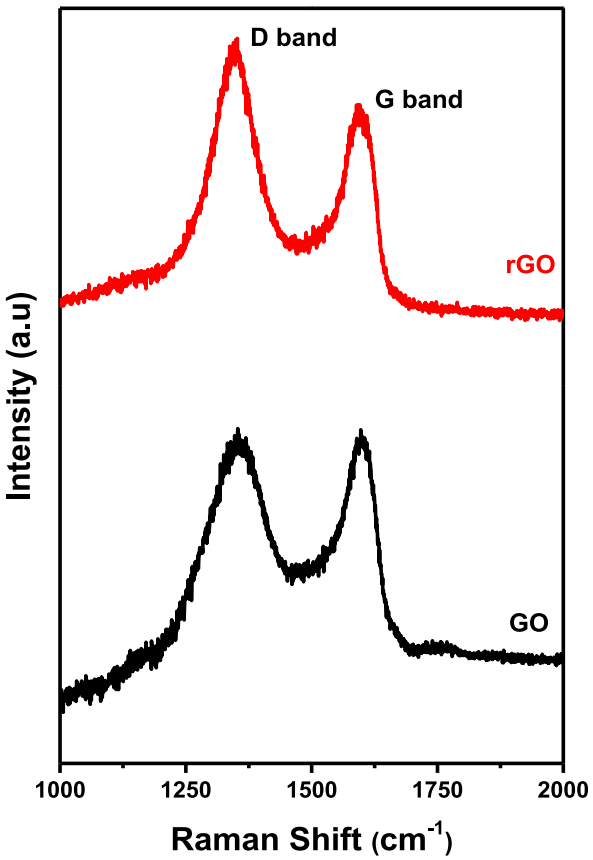

Fig. 8. Raman Spectra of GO and rGO.

due to the semi-conducting properties of hexaferrites. Addition of MWCNT further enhances the electrical conductivity of the polymer composite which is crucial in shielding applications. MWCNT is an excellent conducting material with charge transport efficiency of the order 10^6–10^7 S/m [43]. Conductivity of polymer composite also depends on interaction with neighboring particles. Composites of PANI-coated hexaferrites with MWCNT showed enhanced conductivity in the order of 7.2×10^{-4} S cm^{-1} for the $BaFe_{12}O_{19}$-PANI composite and 4.83×10^{-4} S cm^{-1} for the $SrFe_{12}O_{19}$-PANI composite (Fig. 9). Increased conductivity obtained following the addition of MWCNT to the PANI-coated hexaferrites is essential for effective shielding of EM waves. However, addition of rGO resulted in a negligible change in conductivity (Fig. 9), as rGO is known to have lower intrinsic electrical conductivity compared to MWCNT [48].

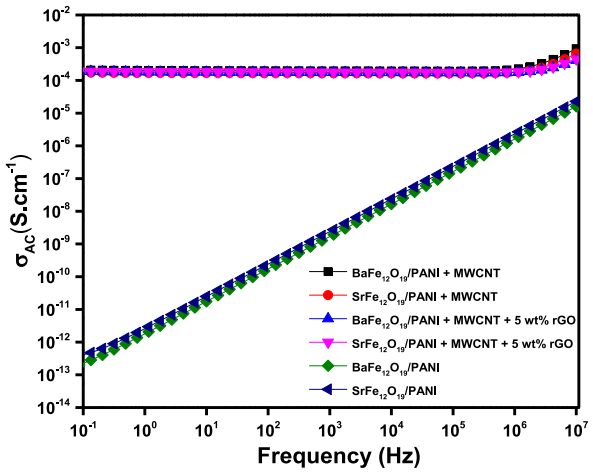

Fig. 9. AC electrical conductivity of the prepared composites.

3.4. EMI shielding effectiveness of prepared composites

EMI shielding is the ability of a material to attenuate the incoming electromagnetic wave, and it is expressed with the unit decibels (dB). Equation (1) gives total shielding effectiveness and is defined as the log of incident power (P_I) to transmitted power (P_T). It is expressed by the following relation [48].

$$SE_T = 10 \log \frac{P_I}{P_T} \tag{1}$$

where P_I is incident power, P_T is transmitted power.

Shielding occurs in a material by three types of mechanisms, shielding by reflection (SE_R), shielding by absorption (SE_A), and shielding by multiple reflections (SE_{MR}) [5,49]. Therefore, total shielding efficiency can be expressed in terms

$$SE_T = SE_R + SE_A + SE_{MR} \tag{2}$$

SE_{MR} can be ignored if the material is having total shielding efficiency greater than 15 dB or the sample thickness is greater than the skin depth of the material represented by equation (3). Therefore, above equation (2) is rewritten as [48].

$$SE_T = SE_R + SE_A \tag{3}$$

experimentally, SE_T, SE_R, SE_A are calculated by equations (4)–(6) respectively, by using the scattering parameters (S_{11}, S_{22}, S_{12}, and S_{21}) obtained from two-port VNA measurement, and their value is derived from the following relations [5].

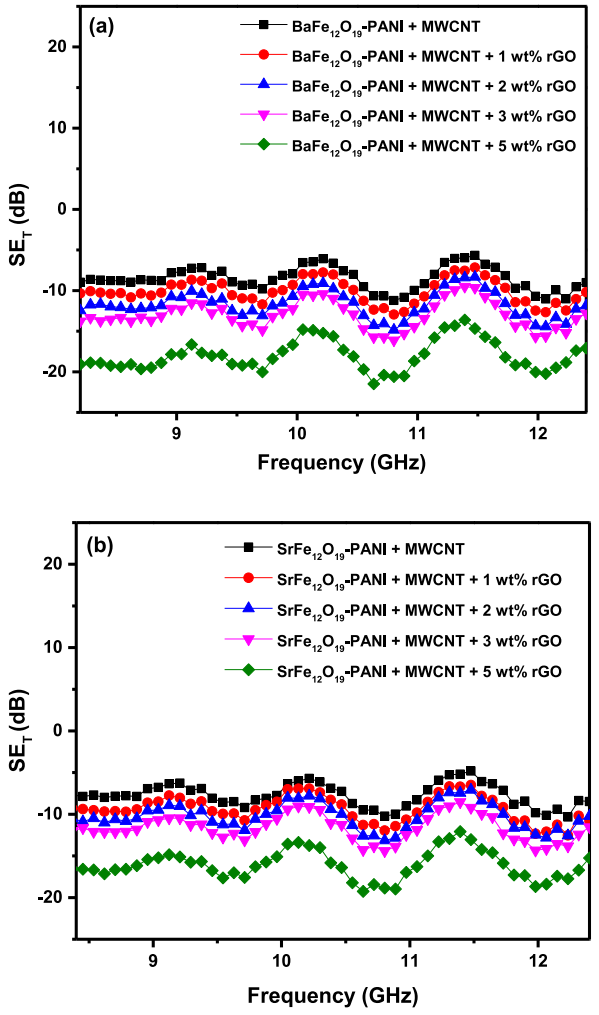

Fig. 10. Total shielding effectiveness of (a) $BaFe_{12}O_{19}$-PANI and rGO/$BaFe_{12}O_{19}$-PANI, and (b) $SrFe_{12}O_{19}$-PANI and rGO/$SrFe_{12}O_{19}$-PANI composites.

$$SE_T = 10 \log \frac{1}{|S_{12}|^2} = 10 \log \frac{1}{|S_{21}|2} \quad (4)$$

$$SE_R = 10 \log \frac{1}{\left(1 - |S_{11}|^2\right)} \quad (5)$$

$$SE_A = 10 \log \frac{\left(1 - |S_{11}|^2\right)}{|S_{21}|^2} = SE_T - SE_R \quad (6)$$

where S_{12}, S_{21} are the reverse and forward transmission coefficients, respectively, and S_{11} is the forward reflection coefficient.

The EM shielding efficacy of $BaFe_{12}O_{19}$-PANI/rGO is higher compared to $BaFe_{12}O_{19}$-PANI composite due to more number of interfaces present in the composite, since EMI property increases with increase in number of interfaces, as well as rGO being semiconducting material and its conductivity depends on the extent of reduction, it shields the EM wave by its free electrons on the surface by impedance mismatch causing reflection, multiple reflection by increasing interface in the composites. Also, rGO shields EM waves by dipole polarization effect due to the C–O functional groups present on its surface. Fig. 10 (a) shows the total shielding effectiveness of the prepared nanocomposites. $BaFe_{12}O_{19}$-PANI composite showed maximum shielding effectiveness of 10.9 dB at 10.6 GHz (Fig. 10a). Addition of rGO increases the shielding effectiveness to 21.5 dB at 10.6 GHz frequency for 5 wt% rGO/$BaFe_{12}O_{19}$-PANI composite (Fig. 10a). This enhancement of shielding effectiveness is attributed to an increase in the number of interfaces and an

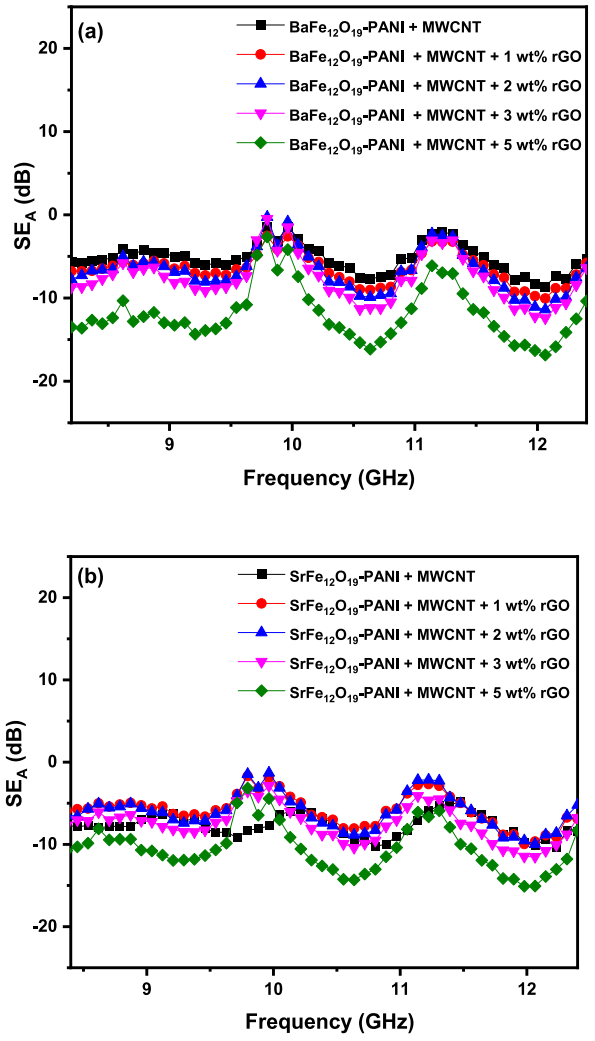

Fig. 11. Shielding effectiveness by absorption of (a) $BaFe_{12}O_{19}$-PANI and rGO/$BaFe_{12}O_{19}$-PANI, and (b) $SrFe_{12}O_{19}$-PANI and rGO/$SrFe_{12}O_{19}$-PANI composites.

increase in the percolation of the composites. Similar trend was observed for rGO/$SrFe_{12}O_{19}$-PANI composites, where the shielding effectiveness increases from 9.9 dB for $SrFe_{12}O_{19}$-PANI to 19.5 dB for 5 wt% of rGO/$SrFe_{12}O_{19}$-PANI composites at 10.6 GHz (Fig. 10b). Fig. 11 depicts the EM shielding that takes place by absorption. The absorptive EM shielding efficacy increased from 7.8 dB for $BaFe_{12}O_{19}$-PANI composite to 16.4 dB for 5 wt% rGO/$BaFe_{12}O_{19}$-PANI (Fig. 11a). Likewise, the EM shielding by absorption increased from 9.4 dB for $SrFe_{12}O_{19}$-PANI composite to 14.4 dB for 5 wt % rGO/$SrFe_{12}O_{19}$-PANI (Fig. 11b). The increased EM absorption associated with the addition of rGO results from an increase in the number of interfaces and the multiple reflections from rGO. Table 2 summarizes the SE_T and SE_A of different weight percentage of rGO/$BaFe_{12}O_{19}$-PANI and rGO/$SrFe_{12}O_{19}$-PANI composites.

Fig. 12(a and b) shows the percentage of absorption and reflection. The absorption efficiency of 1 wt% of rGO/$BaFe_{12}O_{19}$-PANI is 63.9% and that of $BaFe_{12}O_{19}$-PANI is 61.3% (Fig. 12a). It is observed that an increase in the rGO content of the composite by 2 and 3 wt % reduced the absorption percentage to 57.6 and 58.8%, respectively (Fig. 12a). This might be due to reduction in the connectivity of MWCNT by agglomeration and a slight increase in interfacial region. Interestingly, the absorption percentage for 5 wt% rGO/$BaFe_{12}O_{19}$-PANI increased to 66.2% (Fig. 12a). This rise in absorption efficiency might be due to an increase in multiple reflections caused by forming 3-D like network, by providing conducting path, by reducing percolation of MWCNT and by eddy current loss with interaction between magnetic component of the incoming EM wave. Similarly, $SrFe_{12}O_{19}$-PANI showed 66.6% absorption compared to 58.9% for 2 wt% of rGO/$SrFe_{12}O_{19}$-PANI (Fig. 12b). Further increase in rGO content, absorption percentage increases, 5 wt% rGO shows 65% absorption. (Fig. 12b). The similar trend observed in both hexaferrite composites confirms that rGO enhances the total shielding effectiveness and absorption efficiency of composites through conduction loss and polarization loss.

3.5. Shielding of electromagnetic waves by interconnected MWCNT, hexaferrite, and rGO composites

Shielding effectiveness is directly related to MWCNT concentration, as it shields EM waves by charge transport by forming a well-percolated network. MWCNT absorbs EM waves by multiple internal reflections within its network [6]. Adding magnetic particle hexaferrite and rGO to the composite hinders the connectivity and leads to an increase in the percolation path of MWCNT. However, shielding effectiveness is enhanced due to magnetic losses and multiple internal reflections at the interface, which leads to an increase in EM absorption by impedance mismatch in the composite materials [50]. In heterogeneous composites, electric and magnetic parameters are responsible for the shielding of EM wave. Power loss occurs due to microwave heating, which arises from two components of the materials electric field and magnetic field expressed by the following relation.

$$P = \omega \left(\varepsilon_0 \varepsilon''_{eff} {E_{rms}}^2 + \mu_0 \mu''_{eff} {H_{rms}}^2 \right) \tag{7}$$

where P is the power density of the material; E_{rms} and H_{rms} are the electric field and magnetic field strength, respectively; ε_0 represents the permittivity in free space; μ_0 is permeability in a vacuum; ε''_{eff} shows dielectric loss; μ''_{eff} is the imaginary part of magnetic permeability, and ω is the angular frequency of EM wave.

Electric field component absorbs EM wave by conduction loss, interfacial polarization loss, and dipolar polarization loss [7,47]. In MWCNT and rGO-containing composites, electrons will move back and forth in the alternating electric field and induce an electric current, which leads to heating of the sample due to resistance generated by the collision of electrons with each other and with neighboring atoms. Magnetic loss occurs in the composite due to eddy current loss and hysteresis loss [7]. An alternating magnetic field forces the magnetic dipole to align with the magnetic field. The magnetic dipoles are unable to cope with the alternating field, and hence, losses due to resonance become insignificant at higher frequencies.

Based on the above studies, the shielding mechanism is proposed and illustrated in Scheme 3. In a heterogeneous system, various interface and interface charge accumulation sites were created between hexaferrite and PANI. Penetration, diffusion, and recombination occur at the interface between them. Polarons/bipolarons were trapped at the hexaferrite and PANI interfaces when the electrical field was applied due to the dielectric and conductivity difference, forming large dipole centers, which enhances the ability to absorb EM waves by dipolar polarization [51,52]. PANI and hexaferrite create a heterostructure, where the PANI layer acts as a charge carrier; due to the difference in conductivity, electric dipoles are created between PANI and hexaferrite. The electron cloud at the surface of the PANI shell distorts the incoming microwave, which hits the core-shell structure; a strong electric field is formed in opposite to the applied electromagnetic field, then the incident wave diffuses onto the PANI shell surface in the incident direction, and remaining microwaves travel straight through the inner shell of same PANI shell due to insulating property of hexaferrite. Microwaves will reflect at the interface between PANI and hexaferrite because of the difference in conductivity and dielectric constant of PANI and hexaferrite. Additionally, the PANI shell strong electrical conductivity significantly enhances the material's electromagnetic shielding effectiveness. Thus, the conductivity properties of the shell and well-constructed interior contacts are crucial for obtaining optimum shielding performance [53–55].

Table 1
Analysis of the magnetic properties of samples at room temperature.

Sample	Saturation magnetization (Ms) (emu/g)	Coercivity (Hc) (Oe)	Remanent magnetization (Mr) (emu/g)
$BaFe_{12}O_{19}$	49.2	4626	24.1
$BaFe_{12}O_{19}$-PANI	14.8	4626	7.3
$SrFe_{12}O_{19}$	30.4	5284	14.7
$SrFe_{12}O_{19}$-PANI	15.4	3634	7.6

Table 2
Total shielding effectiveness (SE_T) and shielding effectiveness by absorption (SE_A) of Ba-PANI/MWCNT/rGO and Sr-PANI/MWCNT/rGO composites.

Sample	Shielding effectiveness total (SE_T) @ 10.6 GHz	Shielding by Absorption (SE_A) @ 10.6 GHz
$BaFe_{12}O_{19}$-PANI + MWCNT	10.90	7.80
$BaFe_{12}O_{19}$-PANI + MWCNT + 1 wt% rGO	12.60	9.10
$BaFe_{12}O_{19}$-PANI + MWCNT + 2 wt% rGO	14.50	10.20
$BaFe_{12}O_{19}$-PANI + MWCNT + 3 wt% rGO	16.10	11.70
$BaFe_{12}O_{19}$-PANI + MWCNT + 5 wt% rGO	21.50	16.40
$SrFe_{12}O_{19}$-PANI + MWCNT	9.90	9.40
$SrFe_{12}O_{19}$-PANI + MWCNT + 1 wt% rGO	11.60	8.15
$SrFe_{12}O_{19}$-PANI + MWCNT + 2 wt% rGO	12.70	8.90
$SrFe_{12}O_{19}$-PANI + MWCNT + 3 wt% rGO	14.50	10.50
$SrFe_{12}O_{19}$-PANI + MWCNT + 5 wt% rGO	19.50	14.40

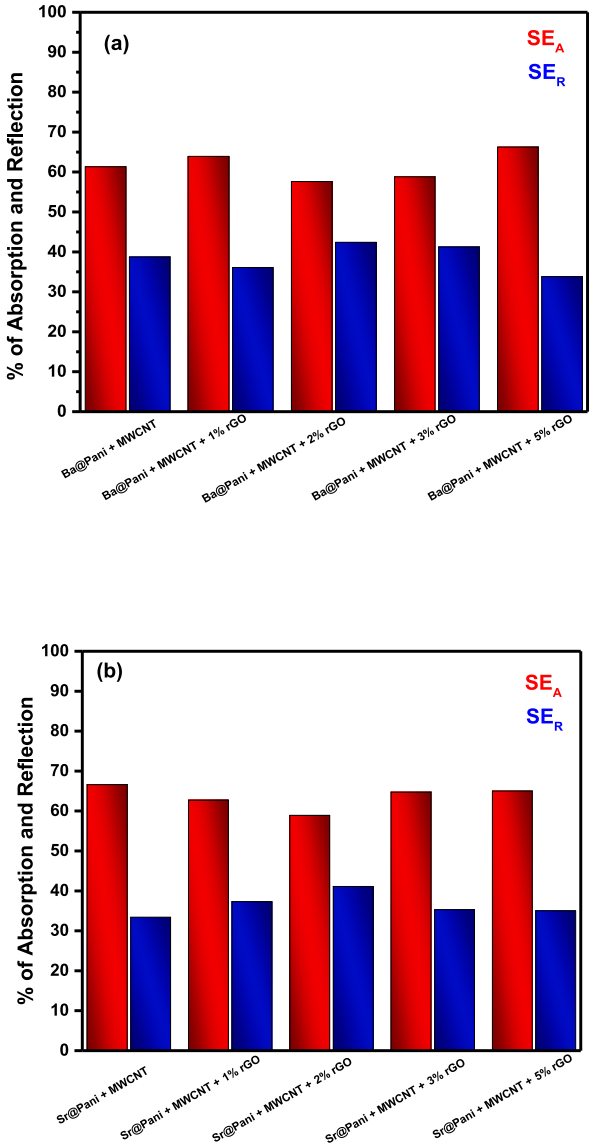

Fig. 12. Percentage absorption and reflection of (a) $BaFe_{12}O_{19}$-PANI and rGO/$BaFe_{12}O_{19}$-PANI and (b) $SrFe_{12}O_{19}$-PANI and rGO/$SrFe_{12}O_{19}$-PANI composites.

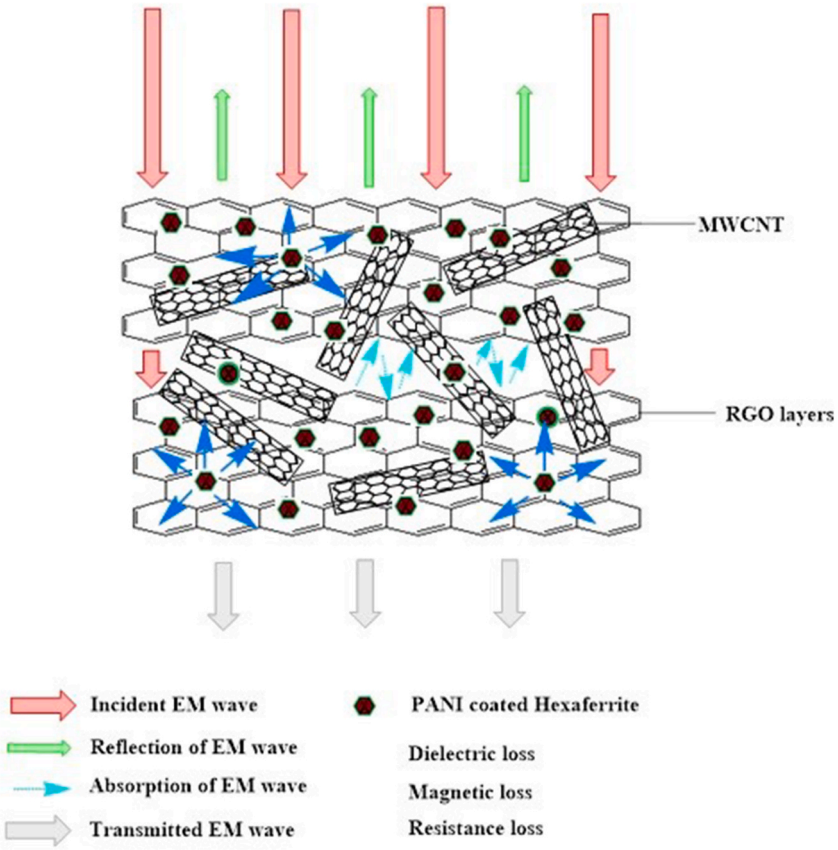

Scheme 3. Shielding Mechanism of EM wave by composite material.

4. Conclusions

We have synthesized rGO by modified Hummer's method. Hexaferrites $BaFe_{12}O_{19}$ and $SrFe_{12}O_{19}$, were synthesized using nitrate citrate gel combustion method, followed by *in situ* polymerization with PANI to form PANI-coated hexaferrites. Structural and morphological properties of the prepared compounds were studied by XRD and SEM characterization techniques. These materials were incorporated in ABS matrix and their EMI shielding efficiency were analyzed. The SE_T value for rGO/$BaFe_{12}O_{19}$-PANI and rGO/$SrFe_{12}O_{19}$-PANI was found to be 21.5 dB and 19.5 dB, respectively. Addition of rGO resulted in an increased SE_T value for both $BaFe_{12}O_{19}$-PANI and $SrFe_{12}O_{19}$-PANI composites by eddy loss, which arises from the interaction of the conducting rGO, PANI-coated hexaferrites and MWCNT with the magnetic component of EM waves. Increased SE_T value of both the rGO/$BaFe_{12}O_{19}$-PANI and rGO/$SrFe_{12}O_{19}$-PANI composites is also aided by interfacial polarization and multiple reflections within the network formed in the composites. Thus, the composites which prepared by inclusion of hybrid nanoparticle will show better shielding behavior compared to individual entity being used.

Author contribution statement

G P Abhilash: Performed the experiments; Analyzed and interpreted the data; Contributed reagents, materials, analysis tools or data; Wrote the paper. Devansh Sharma: Analyzed and interpreted the data; Contributed reagents, materials, analysis tools or data. Suryasarathi Bose: Conceived and designed the experiments; Contributed reagents, materials, analysis tools or data. Shivakumara C: Conceived and designed the experiments; Analyzed and interpreted the data; Contributed reagents, materials, analysis tools or data; Wrote the paper.

Funding statement

CS would like to thank SERB-DST, Government of India, for the financial support under EMEQ (Sanction order EEQ/2016/000691.

Data availability statement

Data included in article/supplementary material/referenced in article.

Declaration of competing interest

The authors declare no conflict of interest.

Acknowledgements

Authors thank the departments of SSCU, Materials Engineering, and CeNSE at the Indian Institute of Science (IISc) for providing the necessary instrumentation facilities.

Appendix A. Supplementary data

Supplementary data to this article can be found online at https://doi.org/10.1016/j.heliyon.2023.e13648.

References

[1] Ding-Xiang Yan, Huan Pang, Bo Li, Robert Vajtai, Ling Xu, Peng-Gang Ren, Jian-Hua Wang, Zhong-Ming Li, Structured reduced graphene oxide/polymer composites for ultra-efficient electromagnetic interference shielding, Adv. Funct. Mater. 25 (4) (2015) 559–566.
[2] Zongping Chen, Chuan Xu, Chaoqun Ma, Wencai Ren, Hui-Ming Cheng, Lightweight and flexible graphene foam composites for high-performance electromagnetic interference shielding, Adv. Mater. 25 (9) (2013) 1296–1300.
[3] Dan He, Yunchuan Xie, Xiao Wang, Zhicheng Zhang, Significantly enhanced electromechanical performance of PDMS crosslinked PVDF hybrids, Polymers 10 (7) (2018) 714.
[4] Om P. Gandhi, Riazi Abbas, Absorption of millimeter waves by human beings and its biological implications, IEEE Trans. Microw. Theor. Tech. 34 (2) (1986) 228–235.
[5] Shital Patangrao Pawar, Sourav Biswas, Goutam Prasanna Kar, Suryasarathi Bose, High frequency millimetre wave absorbers derived from polymeric nanocomposites, Polymer 84 (2016) 398–419.
[6] D.D.L. Chung, Electromagnetic interference shielding effectiveness of carbon materials, Carbon 39 (2) (2001) 279–285.
[7] Jing Sun, Wenlong Wang, Qinyan Yue, Review on microwave-matter interaction fundamentals and efficient microwave-associated heating strategies, Materials 9 (4) (2016) 231.
[8] Aishwarya V. Menon, Giridhar Madras, Suryasarathi Bose, Ultrafast self-healable interfaces in polyurethane nanocomposites designed using diels–alder “click” as an efficient microwave absorber, ACS Omega 3 (1) (2018) 1137–1146.
[9] Jia Huo, Li Wang, Haojie Yu, Polymeric nanocomposites for electromagnetic wave absorption, J. Mater. Sci. 44 (15) (2009) 3917–3927.
[10] Aishwarya V. Menon, Giridhar Madras, Suryasarathi Bose, Magnetic alloy-MWNT Heterostructure as efficient electromagnetic wave suppressors in soft nanocomposites, ChemistrySelect 2 (26) (2017) 7831–7844.
[11] Pulickel Madhavapanicker Ajayan, Nanotubes from carbon, Chem. Rev. 99 (7) (1999) 1787–1800.
[12] Amanuel Gebrekrstos, Sourav Biswas, V. Aishwarya, Menon, Giridhar Madras, Petra Pötschke, and Suryasarathi Bose. "Multi-layered stack consisting of PVDF nanocomposites with flow-induced oriented MWCNT structure can supress electromagnetic radiation, Compos. B Eng. 166 (2019) 749–757.
[13] Mohammad Moniruzzaman, I. Karen, Winey. "Polymer nanocomposites containing carbon nanotubes, Macromolecules 39 (16) (2006) 5194–5205.
[14] Christos Tsonos, Navneet Soin, G. Tomara, Bin Yang, Georgios C. Psarras, Athanasios Kanapitsas, Siores Elias, Electromagnetic wave absorption properties of ternary poly (vinylidene fluoride)/magnetite nanocomposites with carbon nanotubes and graphene, RSC Adv. 6 (3) (2016) 1919–1924.
[15] Xiaofang Liu, Dianjun Zhang, Rongzhi Zhao, Yanhui Zhang, Mu Zhang, Jianjun Wang, Gaowu Qin, Xuefeng Zhang, Tuning microwave absorption properties by hybriding heterogeneous components for core@ shell structural Fe@ SiC flakes, J. Magn. Magn Mater. 462 (2018) 46–52.
[16] Talwinder Kaur, Sachin Kumar, S.B. Narang, A.K. Srivastava, Radiation losses in microwave Ku region by conducting pyrrole/barium titanate and barium hexaferrite based nanocomposites, J. Magn. Magn Mater. 420 (2016) 336–342.
[17] Harish Kumar Choudhary, Rajeev Kumar, Shital Patangrao Pawar, Suryasarathi Bose, Balaram Sahoo, Effect of microstructure and magnetic properties of Ba-Pb-hexaferrite particles on EMI shielding behavior of Ba-Pb-hexaferrite-polyaniline-wax nanocomposites, J. Electron. Mater. 49 (3) (2020) 1618–1629.
[18] Kunal Manna, Suneel Kumar Srivastava, Fe3O4@ carbon@ polyaniline trilaminar core–shell composites as superior microwave absorber in shielding of electromagnetic pollution, ACS Sustain. Chem. Eng. 5 (11) (2017) 10710–10721.
[19] Juhua Luo, Yang Xu, Duoduo Gao, Synthesis, characterization and microwave absorption properties of polyaniline/Sm-doped strontium ferrite nanocomposite, Solid State Sci. 37 (2014) 40–46.
[20] Lei Du, Yunchen Du, Li You, Jingyu Wang, Chao Wang, Xiaohong Wang, Ping Xu, Xijiang Han, Surfactant-assisted solvothermal synthesis of Ba (CoTi) x Fe12− 2 x O19 nanoparticles and enhancement in microwave absorption properties of polyaniline, J. Phys. Chem. C 114 (46) (2010) 19600–19606.
[21] Junliang Liu, Jian Zhang, Yuqing Li, Ming Zhang, Microwave absorbing properties of barium hexa-ferrite/polyaniline core-shell nano-composites with controlled shell thickness, Mater. Chem. Phys. 163 (2015) 470–477.
[22] Han Gao, Chenhui Wang, Zhangjing Yang, Yang Zhang, 3D porous nickel metal foam/polyaniline heterostructure with excellent electromagnetic interference shielding capability and superior absorption based on pre-constructed macroscopic conductive framework, Compos. Sci. Technol. 213 (2021), 108896.
[23] Yang Zhang, Munan Qiu, Ying Yu, Bianying Wen, Lele Cheng, A novel polyaniline-coated bagasse fiber composite with core–shell heterostructure provides effective electromagnetic shielding performance, ACS Appl. Mater. Interfaces 9 (1) (2017) 809–818.
[24] Yang Zhang, Tong Pan, Zhangjing Yang, Flexible polyethylene terephthalate/polyaniline composite paper with bending durability and effective electromagnetic shielding performance, Chem. Eng. J. 389 (2020), 124433.
[25] Zhangjing Yang, Yang Zhang, Bianying Wen, Enhanced electromagnetic interference shielding capability in bamboo fiber@ polyaniline composites through microwave reflection cavity design, Compos. Sci. Technol. 178 (2019) 41–49.
[26] Karthikeyan Krishnamoorthy, Rajneesh Mohan, S.-J. Kim, Graphene oxide as a photocatalytic material, Appl. Phys. Lett. 98 (24) (2011), 244101.
[27] Zheng Bo, Xiaorui Shuai, Shun Mao, Huachao Yang, Jiajing Qian, Junhong Chen, Jianhua Yan, Kefa Cen, Green preparation of reduced graphene oxide for sensing and energy storage applications, Sci. Rep. 4 (1) (2014) 1–8.
[28] Jianfeng Shen, Yizhe Hu, Min Shi, Xin Lu, Chen Qin, Li Chen, Mingxin Ye, Fast and facile preparation of graphene oxide and reduced graphene oxide nanoplatelets, Chem. Mater. 21 (15) (2009) 3514–3520.

[29] Dan Li, Marc B. Müller, Gilje Scott, Richard B. Kaner, Gordon G. Wallace, Processable aqueous dispersions of graphene nanosheets, Nat. Nanotechnol. 3 (2) (2008) 101–105.
[30] A. Mali, A. Ataie, Structural characterization of nano-crystalline BaFe12O19 powders synthesized by sol–gel combustion route, Scripta Mater. 53 (9) (2005) 1065–1070.
[31] Jing Jiang, Lun-Hong Ai, Da-Bin Qin, Hui Liu, Liang-Chao Li, Preparation and characterization of electromagnetic functionalized polyaniline/BaFe12O19 composites, Synth. Met. 159 (7–8) (2009) 695–699.
[32] Xiaoyun Han, Ligang Gai, Haihui Jiang, Lichun Zhao, Hong Liu, Wei Zhang, Core–shell structured Fe3O4/PANI microspheres and their Cr (VI) ion removal properties, Synth. Met. 171 (2013) 1–6.
[33] Yudhajit Bhattacharjee, Dipanwita Chatterjee, Suryasarathi Bose, Core–multishell heterostructure with excellent heat dissipation for electromagnetic interference shielding, ACS Appl. Mater. Interfaces 10 (36) (2018) 30762–30773.
[34] Qinglai Du, Mingbo Zheng, Lifeng Zhang, Yongwen Wang, Jinhua Chen, Luping Xue, Weijie Dai, Guangbin Ji, Jieming Cao, Preparation of functionalized graphene sheets by a low-temperature thermal exfoliation approach and their electrochemical supercapacitive behaviors, Electrochim. Acta 55 (12) (2010) 3897–3903.
[35] Karthikeyan Krishnamoorthy, Murugan Veerapandian, Kyusik Yun, S.-J. Kim, The chemical and structural analysis of graphene oxide with different degrees of oxidation, Carbon 53 (2013) 38–49.
[36] Z.F. Zi, Q.C. Liu, J.M. Dai, Y.P. Sun, Effects of Ce–Co substitution on the magnetic properties of M-type barium hexaferrites, Solid State Commun. 152 (10) (2012) 894–897.
[37] M.M. Hessien, M.M. Rashad, K. El-Barawy, Controlling the composition and magnetic properties of strontium hexaferrite synthesized by co-precipitation method, J. Magn. Magn Mater. 320 (3–4) (2008) 336–343.
[38] Yongchao Si, Edward T. Samulski, Synthesis of water soluble graphene, Nano Lett. 8 (6) (2008) 1679–1682.
[39] Michał Strankowski, Włodarczyk Damian, Łukasz Piszczyk, Justyna Strankowska, Polyurethane nanocomposites containing reduced graphene oxide, FTIR, Raman, and XRD studies, Journal of Spectroscopy (2016) 2016.
[40] Munirah Abdullah Almessiere, Yassine Slimani, N.A. Tashkandi, Abdulhadi Baykal, Mehmet Fahri Saraç, A.V. Trukhanov, Ercan İsmail, İbrahim Belenli, B. Ozçelik, The effect of Nb substitution on magnetic properties of BaFe12O19 nanohexaferrites, Ceram. Int. 45 (2) (2019) 1691–1697.
[41] Ligang Gai, Guojun Du, Zhiyuan Zuo, Yanmin Wang, Duo Liu, Hong Liu, Controlled synthesis of hydrogen titanate− polyaniline composite nanowires and their resistance− temperature characteristics, J. Phys. Chem. C 113 (18) (2009) 7610–7615.
[42] J.I. Paredes, Silvia villar-rodil, amelia martínez-alonso, and juan MD tascon. "Graphene oxide dispersions in organic solvents, Langmuir 24 (2008) 10560–10564, 19.
[43] Karthikeyan Krishnamoorthy, Murugan Veerapandian, Rajneesh Mohan, Sang-Jae Kim, Investigation of Raman and photoluminescence studies of reduced graphene oxide sheets, Appl. Phys. A 106 (3) (2012) 501–506.
[44] A. Abraham, A. Godlyn, E. Manikandan, S. Manikandan, S.K. Vadivel, A. Baykal Jaganathan, P. Sri Renganathan, Enhanced magneto-optical and photo-catalytic properties of transition metal cobalt (Co2+ ions) doped spinel MgFe2O4 ferrite nanocomposites, J. Magn. Magn Mater. 452 (2018) 380–388.
[45] Xiaohu Ren, Xilou Pu, Hongfeng Yin, Yun Tang, Hudie Yuan, Huiqing Fan, Fabrication of hierarchical PANI@ W-type barium hexaferrite composites for highly efficient microwave absorption, Ceram. Int. 47 (9) (2021) 12122–12129.
[46] Yinyun Lü, Yiting Wang, Hongli Li, Lin Yuan, Zhiyuan Jiang, Zhaoxiong Xie, Kuang Qin, Lansun Zheng, MOF-derived porous Co/C nanocomposites with excellent electromagnetic wave absorption properties, ACS Appl. Mater. Interfaces 7 (24) (2015) 13604–13611.
[47] S. Abdalla, F. Al-Marzouki, Ahmed A. Al-Ghamdi, A. Abdel-Daiem, Different technical applications of carbon nanotubes, Nanoscale Res. Lett. 10 (1) (2015) 1–10.
[48] Kumari Sushmita, Aishwarya V. Menon, Shubham Sharma, Ashutosh C. Abhyankar, Giridhar Madras, and Suryasarathi Bose. "Mechanistic insight into the nature of dopants in graphene derivatives influencing electromagnetic interference shielding properties in hybrid polymer nanocomposites, J. Phys. Chem. C 123 (4) (2019) 2579–2590.
[49] Shielding Geetha, K. K. Satheesh Kumar, Chepuri Rk Rao, M. Vijayan, D.C. Trivedi, EMI shielding: methods and materials—a review, J. Appl. Polym. Sci. 112 (4) (2009) 2073–2086.
[50] Devansh Sharma, Aishwarya V. Menon, Suryasarathi Bose, Graphene templated growth of copper sulphide 'flowers' can suppress electromagnetic interference, Nanoscale Adv. 2 (8) (2020) 3292–3303.
[51] Xiaoling Luo, Guanda Yang, Dirk W. Schubert, Electrically conductive polymer composite containing hybrid graphene nanoplatelets and carbon nanotubes: synergistic effect and tunable conductivity anisotropy, Advanced Composites and Hybrid Materials 5 (2022) 250–262, 1.
[52] Yang Zhang, Zhangjing Yang, Bianying Wen, An ingenious strategy to construct helical structure with excellent electromagnetic shielding performance, Adv. Mater. Interfac. 6 (2019), 1900375, 11.
[53] Xiaoling Luo, Guanda Yang, Dirk W. Schubert, Electrically conductive polymer composite containing hybrid graphene nanoplatelets and carbon nanotubes: synergistic effect and tunable conductivity anisotropy, Advanced Composites and Hybrid Materials 5 (2022) 250–262, 1.
[54] Yang Zhang, Zhangjing Yang, Tong Pan, Han Gao, Hongtao Guan, Jianzhe Xu, Zhenyu Zhang, Construction of natural fiber/polyaniline core-shell heterostructures with tunable and excellent electromagnetic shielding capability via a facile secondary doping strategy, Compos. Appl. Sci. Manuf. 137 (2020), 105994.
[55] Chenhui Wang, Han Gao, Dongming Liang, Shuai Liu, Huijuan Zhang, Hongtao Guan, Yuxuan Wu, Yang Zhang, Effective fabrication of flexible nickel chains/acrylate composite pressure-sensitive adhesives with layered structure for tunable electromagnetic interference shielding, Advanced Composites and Hybrid Materials (2022) 1–15.